Design, synthesis and biological evaluation of novel 9-*N*-substituted-13-alkylberberine derivatives from Chinese medicine as anti-hepatocellular carcinoma agents

Jichao Chen [a,*], Yiping Duan [b], Kan Yang [c], Jiahe Wang [a], Junjie Yan [a], Chenglei Gu [a], Shanglong Wang [a], Zheying Zhu [d], E-Hu Liu [a,*], Jinyi Xu [b,*]

[a] School of Pharmacy, Nanjing University of Chinese Medicine, Nanjing 210023, China

[b] State Key Laboratory of Natural Medicines and Department of Medicinal Chemistry, China Pharmaceutical University, 24 Tong Jia Xiang, Nanjing 210009, China

[c] Key Laboratory of Pharmaceutical Quality Control of Hebei Province, College of Pharmaceutical Sciences, Hebei University, Baoding, 071002, China

[d] Division of Molecular Therapeutics & Formulation, School of Pharmacy, the University of Nottingham, University Park Campus, Nottingham NG7 2RD, U.K.

[*]**Corresponding authors:** E-Mail: chenjichao@njucm.edu.cn (J. Chen); E-Mail: liuehu2011@163.com (E. Liu); E-Mail: jinyixu@china.com (J. Xu).

ABSTRACT

A series of novel 9-*N*-substituted-13-alkylberberine derivatives from Chinese medicine were designed and synthesized with improved anti-hepatocellular carcinoma (HCC) activities. The optimal compound **4d** showed strong activities against HepG2, Sk-Hep-1, Huh-7 and Hep3B cells with IC_{50} values of 0.58~1.15 μM, which were superior to positive reference cisplatin. Interestingly, **4d** exhibited over 40-fold more potent activity against cisplatin-resistant HepG2/DPP cells while showing lower cytotoxicity in normal LX-2 cells. The mechanism studies revealed **4d** greatly stabilized G-quadruplex DNA leading to intracellular *c*-MYC expression downregulation, blocked G2/M-phase cell cycle by affecting related *p*-cdc25c, cdc2 and cyclin B1 expressions, and induced apoptosis by a ROS-promoted PI3K/Akt-mitochondrial pathway. Furthermore, **4d** possessed good pharmacokinetic properties and significantly inhibited the tumor growth in the H22 liver cancer xenograft mouse model without obvious toxicity. Altogether, the remarkably biological profiles of **4d** both *in vitro* and *in vivo* would make it a promising candidate for HCC therapy.

KEYWORDS

Hepatocellular carcinoma; Berberine; G-quadruplex DNA; Mitochondrial dysfunction; PI3K/Akt pathway

1. Introduction

Natural products (NPs) act as the lasting importance in the research and development of anticancer drugs[1]. In addition to themselves as new chemical entities (NCEs) for cancer therapy, NPs also provide potential lead compounds for the development of new antitumor drugs through structural modification[2,3]. Over the past nearly four decades from 1981 to 2019, NPs and related compounds accounted for more than 80% of the approved antitumor small-molecule drugs[4]. Many synthetic antitumor molecules in clinic are unfavorable due to their resistance, toxicity and adverse effects, while NP-derived drugs are generally characterized by low toxicity and high safety[5]. Hence, there is always a requirement to search for novel, safe and more effective anticancer agents from NPs.

Berberine (**1**, Figure 1), a plant-derived natural product, has traditionally been used to treat gastrointestinal disorders such as bacillary dysentery in China[6]. Moreover, berberine has been reported to possess diverse pharmacological activities such as antimicrobial, anti-depressant, anti-Alzheimer, anti-obesity, antiviral, anti-hypertensive, anti-inflammatory, hypoglycemic, hypolipidemic, *etc*[7-11]. In recent years, increasing attention has been paid to berberine's anticancer activity[12], and in particular, plenty of efforts have been devoted berberine to preventing and treating hepatocellular carcinoma (HCC). Studies have demonstrated that berberine could suppress the growth of multiple hepatoma cells while showing lower cytotoxicity in normal cells[13-15]. Besides, combination of radiotherapy/chemotherapy treatments with berberine could decrease the toxicity and even strengthen the antitumor efficacy[16-18]. Thus, Chinese medicine berberine seems to be a good lead compound for the development of new anti-HCC drugs, although the poor solubility and moderate anticancer potency need to be improved[19].

G-quadruplex (G4) DNA, a secondary four-stranded structure formed by varying guanine-rich DNA sequences, has been considered a promising cancer-specific target[20,21]. That, especially produced in human oncogenes (*e.g. c*-MYC) and telomeres, plays important roles in the proliferation, apoptosis, migration, invasion and metastasis of tumor cells[20-22]. The overexpression of *c*-MYC gene is associated with various human malignancies, which may be restrained by stabilization of ligand-mediated *c*-MYC G4s[23,24]. G4 stabilization by a small-molecule ligand could repress the transcription of *c*-MYC gene and/or induce DNA damage at *c*-MYC gene, leading to replication defects and cancer cell death[21,23,24]. It has been reported that berberine exerts anticancer activity related to its *c*-MYC G4-stabilizing effect[25,26]. And berberine showed higher binding affinity toward G4 DNA than duplex DNA[27,28]. Furthermore, recent studies demonstrated that the level of G4 formation was markedly upregulated in human liver cancer tissues[29]. As a consequence, targeting G4 with berberine as lead compound via structural modification could be a promising manner for anti-HCC drug development.

Very recently, we reported a series of 9-*O*-aminoalkyl-13-octylberberine derivatives with improved *c*-MYC G4 stabilization and anti-HCC potency (*Previous work*, Figure 1)[30]. In our ongoing efforts on the development of 9,13-disubstituted

berberine derivatives for more effective anti-HCC agents, a series of novel 9-*N*-substituted-13-alkylberberine derivatives were further designed with the strategies as follows (*This work*, Figure 1): 1) bioisosteric replacement (BR) of 9-*O* with 9-*N*; 2) BR of amino with hydroxyl group or without; 3) 8,9-position cyclization after determining the optimal amino or hydroxyl group; 4) optimization of 13-alkyl group after obtaining the most potent 9-*N*-13-octylberberine derivative with or without cyclization. Herein, we would like to report the work of the synthesis, *in vitro* antiproliferative activity, anti-HCC mechanism, and *in vivo* pharmacokinetic/efficacy studies for these 9-*N*-13-disubstituted berberine derivatives from Chinese medicine.

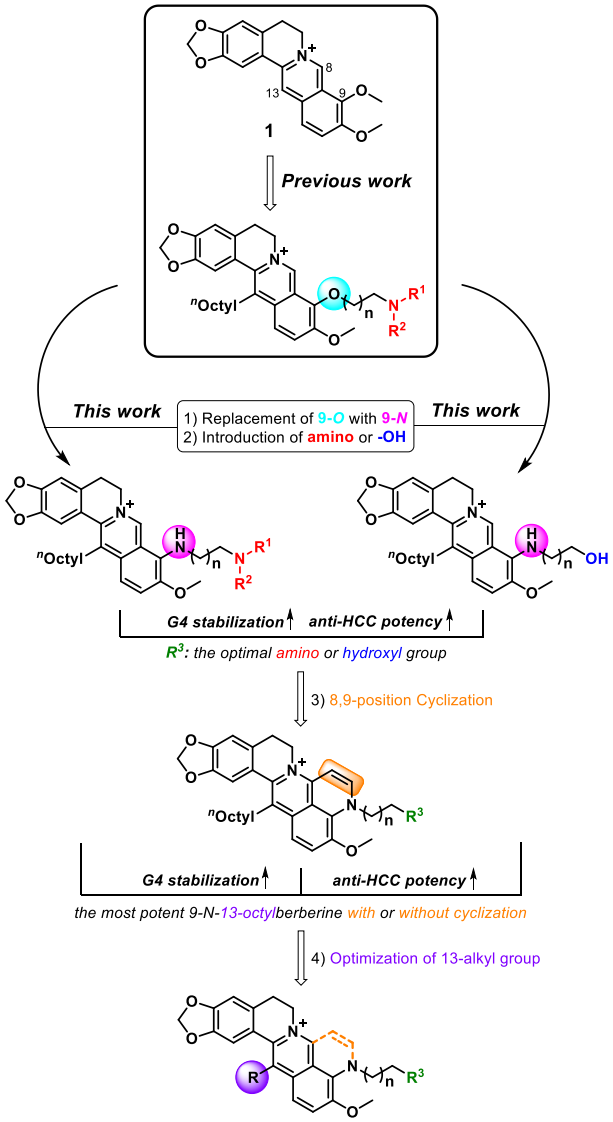

Figure 1. Design strategies of novel 9-*N*-substituted-13-alkylberberine derivatives

2. Results and discussion

2.1. Chemistry

The synthetic routes of compounds **4a-f** or **5** are shown in Scheme 1. Reduction of berberine (**1**) with $NaBH_4$ under the base gave compound **2**, which was then treated with *n*-octanal in a mixed solvent of EtOH/AcOH to form compound **3a**. Next, **3a** was

reacted with different amines or 2-aminoethanol using dry acetonitrile as solvent to afford the title compounds **4a-f** or **5**.

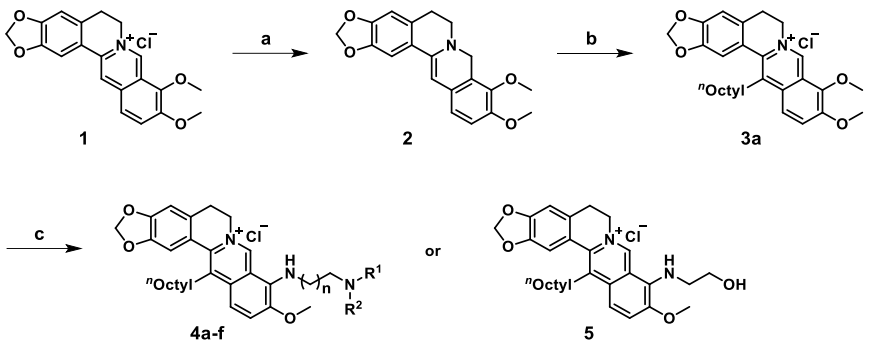

Scheme 1. Synthesis of compounds **4a-f** or **5**. Reagents and conditions: (a) $NaBH_4$, 5% NaOH, K_2CO_3, MeOH, rt, 2 h; (b) n-octanal, AcOH, 80% EtOH, 90 °C, 6 h, then 1N HCl, rt, 2 h; (c) amines or 2-aminoethanol, CH_3CN, reflux, 7-12 h.

The synthetic route of compound **6a** or **6b** is illustrated in Scheme 2. Reaction of **3a** with *N*,*N'*-dimethylethylenediamine or 2-aminoethanol using anhydrous ethanol as solvent under reflux produced the title compound **6a** or **6b**.

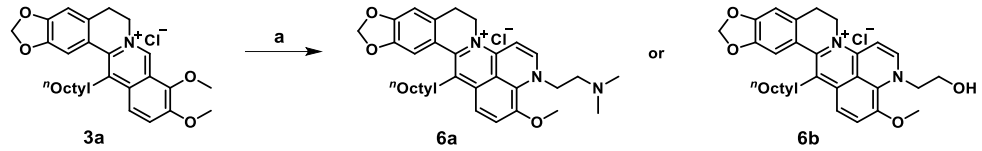

Scheme 2. Synthesis of compound **6a** or **6b**. Reagents and conditions: (a) *N*,*N'*-dimethylethylenediamine or 2-aminoethanol, EtOH, reflux, 18 h.

The synthetic routes of compounds **7a-c** or **8a-c** are displayed in Scheme 3. Compound **2** was reacted with different aldehydes using EtOH/AcOH as solvent to form compound **3b-d**, followed by treatment with *N*,*N'*-dimethylethylenediamine or 2-aminoethanol using dry acetonitrile as solvent to give the title compounds **7a-c** or **8a-c**.

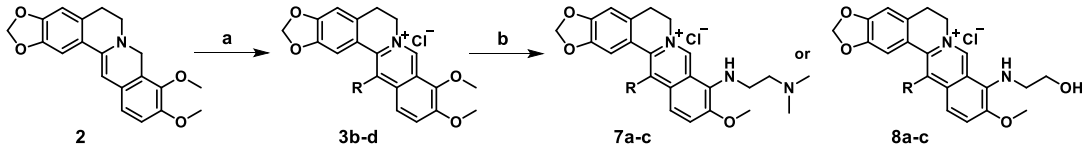

Scheme 3. Synthesis of compounds **7a-c** or **8a-c**. Reagents and conditions: (a) RCHO, AcOH, 80% EtOH, 90 °C, 5-8 h, then 1N HCl, rt, 2 h; (b) *N*, *N'*-dimethylethylenediamine or 2-aminoethanol, CH_3CN, reflux, 7-10 h.

2.2. Antiproliferative activity against HepG2 cells

Compounds **4a-c** were initially prepared with a free amino group and their antiproliferative activity was examined in HepG2 cells. The results were summarized in Table 1. As expected, these compounds showed significantly improved anti-HCC activity (IC_{50} 5.17 ~ 8.61 μM) compared to parent compound berberine (IC_{50} > 50 μM). Meanwhile, it was found that the chain length had little effect on the activity by

extending from C_2 to C_4 (*e.g.* **4a** *vs* **4b** *vs* **4c**). Replacement of the free amino group with a substituted one such as dimethylamino, pyrrolidinyl, morpholinyl group led to the syntheses of compounds **4d-f** with markedly enhanced activity, in particular, compound **4d** showed the most potent activity with an IC_{50} value of 0.64 μM (Table 1). On the other hand, when the free amino group was substituted with a hydroxyl group (**5**), the activity also increased with an IC_{50} value of 2.76 μM (Table 1).

Selected compounds **4d** and **5** then underwent 8,9-cyclization to further explore the structure-activity relationships. The bioassay results indicated the obtained compounds **6a** and **6b** possessed comparable activity to the corresponding compounds before cyclization with IC_{50} values of 1.01 μM and 2.28 μM (Table 1), respectively, suggesting the cyclization had no effect on the activity. Next, C13-octyl group of **4d** and **5** was optimized with alkyl groups of diverse lengths, however, the resulting compounds **7a-c** and **8a-c** didn't show higher activity with IC_{50} values from 1.02 to 2.42 μM and 2.03 to 4.52 μM (Table 1), respectively.

Altogether, compound **4d** exhibited the strongest activity against HepG2 cells among all the synthesized derivatives, which was over 10 times more potent than positive control cisplatin (Table 1).

Table 1. Antiproliferative activity of berberine derivatives against HepG2 cells

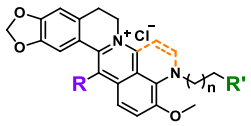

Compd	R	n	R'	IC_{50}[a] (μM)
berberine	/	/	/	> 50
4a	^{n}octyl	1	$-NH_2$	8.61 ± 0.52
4b	^{n}octyl	2	$-NH_2$	7.18 ± 0.45
4c	^{n}octyl	3	$-NH_2$	5.17 ± 0.35
4d	^{n}octyl	1	$-N(CH_3)_2$	0.64 ± 0.06
4e	^{n}octyl	2		1.37 ± 0.14
4f	^{n}octyl	2		1.12 ± 0.09
5	^{n}octyl	1	-OH	2.76 ± 0.18
6a[b]	^{n}octyl	1	$-N(CH_3)_2$	1.01 ± 0.06
6b[b]	^{n}octyl	1	-OH	2.28 ± 0.19
7a	^{n}hexyl	1	$-N(CH_3)_2$	2.42 ± 0.16
7b	^{n}decyl	1	$-N(CH_3)_2$	1.02 ± 0.08
7c	^{n}dodecyl	1	$-N(CH_3)_2$	1.24 ± 0.12
8a	^{n}hexyl	1	-OH	4.52 ± 0.33
8b	^{n}decyl	1	-OH	2.03 ± 0.14
8c	^{n}dodecyl	1	-OH	2.31 ± 0.21
cisplatin	/	/	/	7.52 ± 0.43

[a] Concentration of test compound that inhibits 50% of cell growth. [b] Compound with 8,9-cyclization. Data are expressed as the mean ± SD (n = 3).

2.3. Antiproliferative activity of compound 4d against a wide range of hepatoma cell lines

The anti-HCC activity of compound **4d** was further tested against four hepatoma cell lines including Sk-Hep-1, Huh-7, Hep3B and cisplatin-resistant HepG2/DDP cells. As presented in Table 2, **4d** displayed strong antiproliferative activities against Sk-Hep-1, Huh-7 and Hep3B cells with IC_{50} values from 0.58 to 1.15 μM, which were much more potent than berberine with IC_{50} values of > 50 μM, and even significantly superior to that of cisplatin with IC_{50} values from 4.53 to 10.36 μM. Interestingly, **4d** showed more than 40-fold higher activity (IC_{50} 2.12 μM) against HepG2/DDP cells than cisplatin (IC_{50} 87.02 μM, Table 2), whereas exhibiting lower cytotoxicity against normal hepatic LX-2 cells compared to selected hepatoma cell lines (Table 2). Therefore, compound **4d** was chosen for subsequent anti-HCC mechanism and further *in vivo* pharmacokinetic/efficacy studies.

Table 2. Antiproliferative activities of compound **4d** against five hepatic cell lines

Compd	IC_{50}[a] (μM)				
	Sk-Hep-1	Huh-7	Hep3B	HepG2/DDP[b]	LX-2
berberine	> 50	> 50	> 50	> 50	> 50
4d	1.07 ± 0.09	0.58 ± 0.05	1.15 ± 0.07	2.12 ± 0.13	8.62 ± 0.51
cisplatin	7.14 ± 0.46	4.53 ± 0.38	10.36 ± 0.65	87.02 ± 1.40	7.76 ± 0.37

[a] Concentration of test compound that inhibits 50% of cell growth. [b] Cisplatin-resistant HepG2 cells. Data are expressed as the mean ± SD (n = 3).

2.4. G4-binding activity of selected compounds 4d-f, 6a

To explore whether the excellent anti-HCC activity of the obtained derivatives was related to G4 stabilization, the fluorescent FPu18T and F10T were separately treated as *c*-MYC G4 and duplex DNA models in FRET-melting assays with berberine as a reference. The results were displayed in Table 3. All the selected compounds showed notably enhanced G4-binding effects (ΔT_m 18.5~23.1°C) compared to berberine (ΔT_m 1.6 °C). The melting temperature of F10T was also checked, and no obvious changes were made by **4d**, **4f** and **6a** with ΔT_m values of 0.2~0.6 °C except for **4e** with a slightly higher ΔTm value of 1.8 °C (Table 3).

In order to further investigate the selectivity of selected compounds toward G4 DNA, the nonfluorescent duplex DNA (ds26) was employed as a competitor in FRET-based competition experiments. As seen in Table 3, the melting temperature (ΔT_m 17.4~ 21.1 °C) of FPu18T stabilized by **4d**, **4f**, **6a** was not obviously altered in the presence of excess ds26, suggesting the duplex DNA had little effect on the G4 binding of these derivatives, although the stabilization temperature by **4e** was mildly influenced with a ΔT_m value of 19.3 °C.

The above results demonstrated the synthesized derivatives could greatly stabilize G4 DNA with high selectivity. In particular, compound **4d** showed the lowest binding affinity toward duplex DNA with a ΔT_m value of 0.2 °C and maintained a similar G4-stabilizing temperature in the absence or presence of excess duplex DNA (ΔT_m 21.4 *vs* 20.9 °C, Table 3), which was also consistent with its strong anti-HCC activity, suggesting high *c*-MYC G4-binding potency may contribute to enhancing the anti-HCC activity.

Table 3. DNA-stabilizing temperatures of selected compounds

Compd	ΔT_m [a] (°C)	ΔT_m [b] (°C)	ΔT_m [c] (°C)
berberine	1.6	2.1	/
4d	21.4	0.2	20.9
4e	23.1	1.8	19.3
4f	18.5	0.6	17.4
6a	21.8	0.4	21.1

[a]ΔT_m = T_m (FPu18T + Compd) - T_m (FPu18T). [b]ΔT_m = T_m (F10T + Compd) - T_m (F10T).
[c]ΔT_m = T_m (FPu18T + Compd) - T_m (FPu18T) in the presence of excess ds26.

2.5. Docking studies of compound 4d with *c*-MYC G4 DNA

Compound **4d** was selected to further investigate the binding effect with *c*-MYC G4 DNA by molecular docking calculation using AutoDock 4.2[31]. Conformation superposition revealed that **4d** showed a similar binding mode to the original ligand (*N*,*N*-diethyl-*N'*-(10H-indolo[3,2-b]quinolin-11-yl)ethane-1,2-diamine) with a binding energy of about -7.4 kcal/mol. The large rigid scaffolds of two compounds were partially superimposed in the binding groove (Figure 2A). The aromatic plane of **4d** inserted into the crack and formed strong π-π stacking contacts with G5 and G16 (Figure 2B), which might contribute to **4d**'s high G4-stabilizing effect. Besides, the side chain bearing a dimethyl amino group positioned toward the ribose of G12, while the alkyl chain inserted into the small space between G17 and G20, holding the target like two arms (Figure 2B). These results indicated that **4d** possessed high binding affinity toward *c*-MYC G4 DNA.

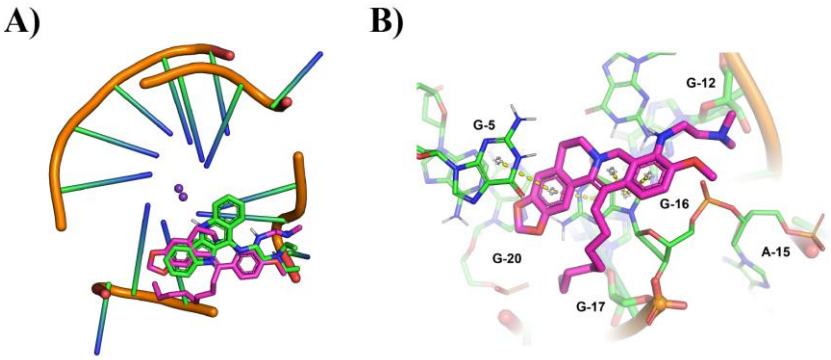

Figure 2. Proposed binding mode (A) and binding site (B) of compound **4d** with *c*-MYC G4 DNA (PDB ID: 2L7V) analyzed by molecular docking. **4d** is shown in purple, original ligand in green.

2.6. Compound 4d induced G4 formation leading to *c*-MYC expression downregulation in cells

To study the interaction of compound **4d** with G4 DNA in HepG2 cells, the immunocytochemistry assay with G4-binding BG4 antibody was carried out[32]. As shown in Figure 3A, **4d** induced more BG4 foci formation and colocalized with BG4 in the G4-forming region (red in color). These results indicated that **4d** could markedly induce and stabilize G4 DNA formation in HepG2 cells.

Accumulating evidence demonstrated that the ligand-mediated G4 stabilization could suppress the transcription of *c*-MYC gene in cancer cells[23,24]. Thus, western blot

assay was performed to examine *c*-MYC expression in **4d**-treated HepG2 cells (Figure 3B). As seen in Figure 3C, **4d** could observably decrease the level of *c*-MYC expression in a concentration-dependent manner. The results suggested that **4d** could significantly downregulate *c*-MYC expression in HepG2 cells, which was probably associated with **4d**-mediated G4 stabilization.

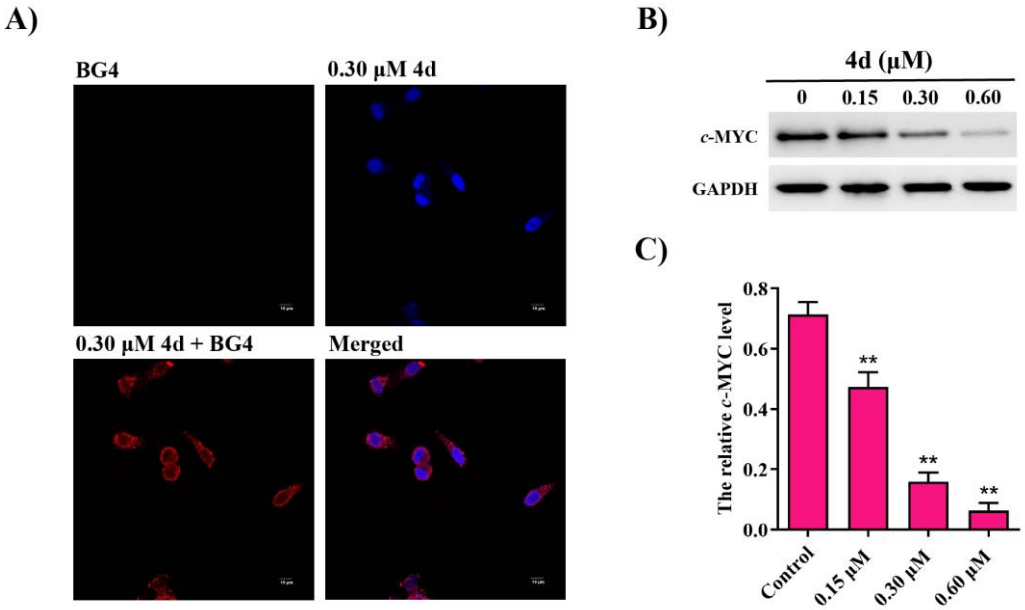

Figure 3. Compound **4d** colocalized with G4 DNA and downregulated c-MYC expression in HepG2 cells. (A) Representative images of immunocytochemistry with BG4 antibody. Scale bar = 10 μm. (B) Western blot analysis of *c*-MYC expression with GAPDH as internal reference. (C) Histograms display the density ratio of *c*-MYC to GAPDH. Data are expressed as the mean ± SD (n = 3). $^{**}p < 0.01$ *vs.* control group.

2.7. Compound 4d induced G2/M-phase cell cycle arrest with related protein expression changes

It was reported that a lot of G4 conformations existed in *c*-MYC oncogene region to keep the stable DNA replication action[33]. Thus, to investigate whether compound **4d** influenced the cell cycle progression, HepG2 cells were incubated with **4d** at diverse concentrations, the G2-phase cell percentages increased from 12.99% to 27.61%, while the S-phase cell percentages concomitantly decreased from 35.98% to 21.63% (Figure 4A,B), indicating that **4d** concentration-dependently induced G2/M-phase cell cycle arrest. Furthermore, the G2/M-phase cell cycle arrest in eukaryotic cells might be regulated by few relevant proteins such as cdc25c, cdc2, cyclin B1[34]. As illustrated in Figure 4C,D by western blot analysis, compound **4d** dose-dependently up-regulated the expression of *p*-cdc25c and down-regulated the expressions of cdc2 and cyclin B1. The results indicated that **4d** induced G2/M-phase cell cycle arrest probably by affecting the expressions of related *p*-cdc25c, cdc2 and cyclin B1 proteins.

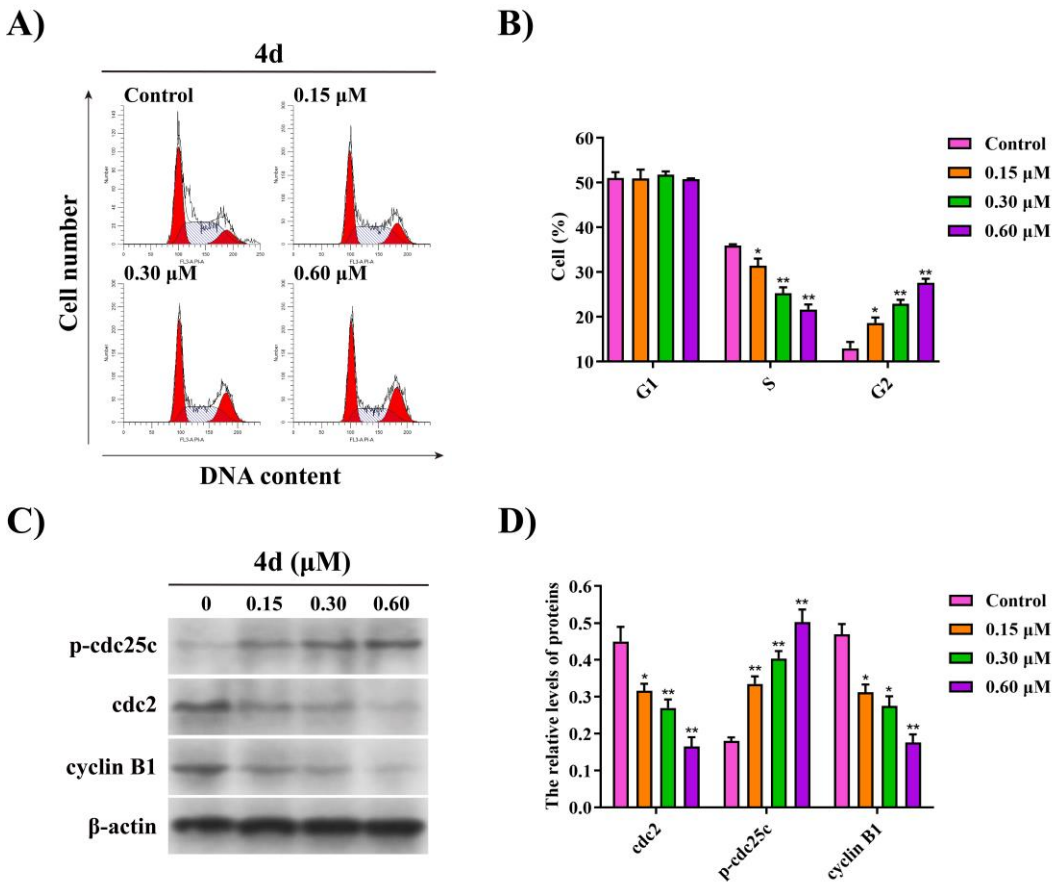

Figure 4. Compound **4d** induced G2/M-phase cell cycle arrest with related protein expression changes. (A) Representative images of cell cycle analyzed by flow cytometry. (B) Histograms display the percentages of cell cycle distribution. (C) Western blot analysis of G2/M-phase related proteins with *β*-actin as internal reference. (D) Histograms display the density ratios of *p*-cdc25c, cdc2 and cyclin B1 to *β*-actin. Data are expressed as the mean ± SD (n = 3). **p* < 0.05, ***p* < 0.01 *vs*. control group.

2.8. Compound 4d induced cell apoptosis with related protein expression changes

Several studies revealed that ligand-mediated *c*-MYC G4 stabilization could trigger tumor cell apoptosis[35-37]. To check whether compound **4d** induced HepG2 cell apoptosis, after treatment with diverse concentrations of **4d**, the percentages of total apoptotic cells increased from 4.10% to 51.25% (Figure 5A,B), suggesting that **4d** significantly induced apoptosis of HepG2 cells in a concentration-dependent manner. It's well known that the occurrence of apoptosis is probably mediated through a mitochondrial-dependent pathway[38]. Thus, the related proteins such as Bax, Bcl-2, cytochrome C, caspase-3 were tested in HepG2 cells by western blot analysis. After incubation with **4d** for 72 h, the levels of Bax, cytochrome C and cleaved caspase-3 expressions markedly increased in dose-dependent manners, while the Bcl-2 expression level decreased concomitantly (Figure 5C,D).

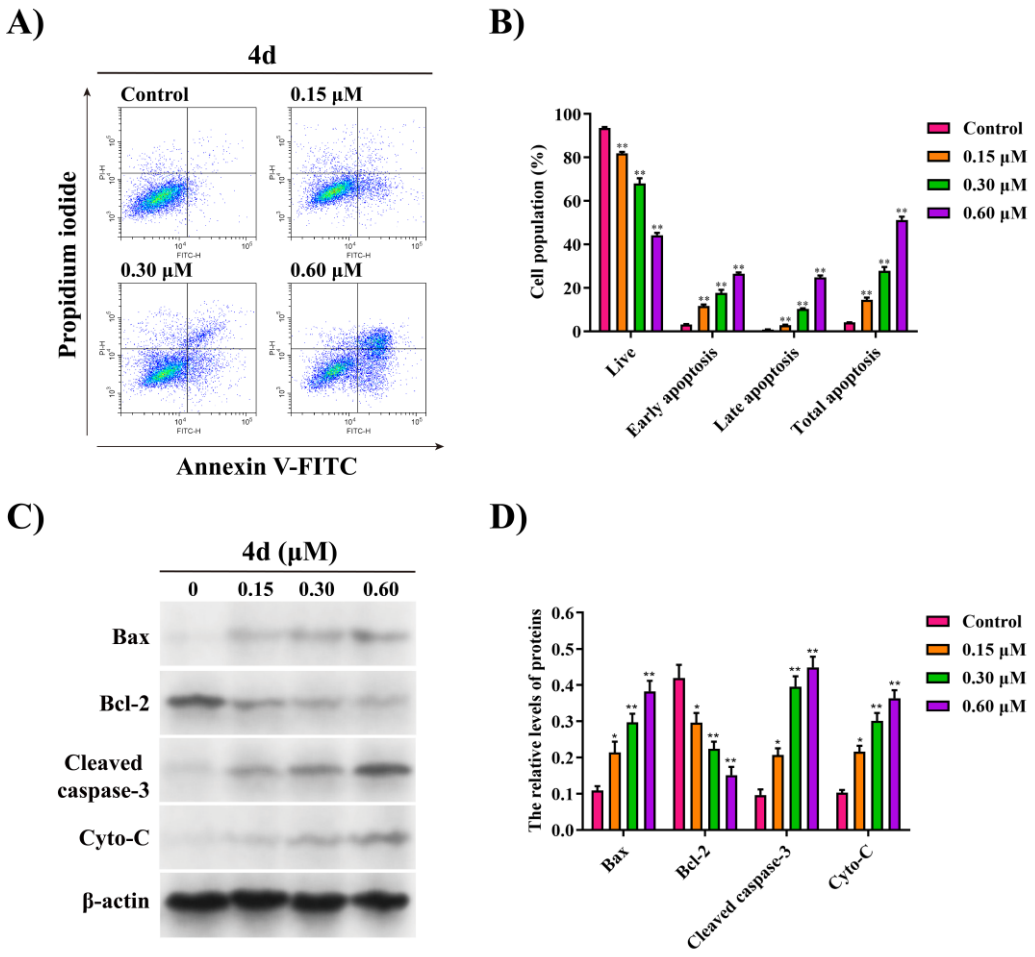

Figure 5. Compound **4d** induced cell apoptosis with related protein expression changes. (A) Representative images of cell apoptosis analyzed by flow cytometry. (B) Histograms display the cell distribution percentages. (C) Western blot analysis of apoptosis-related proteins with *β*-actin as internal reference. (D) Histograms display the density ratios of Bax, Bcl-2, Cyto-C and cleaved caspase-3 to *β*-actin. Cyto-C: cytochrome C. Data are expressed as the mean ± SD (n = 3). **p* < 0.05, ***p* < 0.01 *vs.* control group.

2.9. Compound 4d promoted ROS-mediated PI3K/Akt-mitochondrial pathway

It has been widely proved that ROS accumulation is a major factor in inducing apoptosis and mitochondrial dysfunction[39,40]. To examine whether compound **4d** influenced ROS contents in HepG2 cells, after incubation with **4d** at concentrations of 0~0.60 μM, the percentages of ROS-positive cells increased from 4.21% to 52.48% (Figure 6A,B), however, which was completely restrained by pre-incubation with *N*-acetyl cysteine (NAC, 1.0 mM) as a ROS scavenger (3.67%, Figure 6A,B). The results indicated that HepG2 cell apoptosis could be mediated by **4d**-promoted ROS production.

HepG2 cell apoptosis induced by **4d** is likely involved in a mitochondrial pathway based on the above results. Mitochondrial depolarization is an initiating step in the process of apoptosis[38]. To investigate whether **4d** triggered mitochondrial dysfunction, after treatment with **4d** at indicated concentrations, the percentages of HepG2 cells with collapsed mitochondrial membrane potential (MMP) dose-dependently increased from

4.84% to 40.73% (Figure 6C,D), indicating that **4d** induced mitochondrial depolarization and dysfunction.

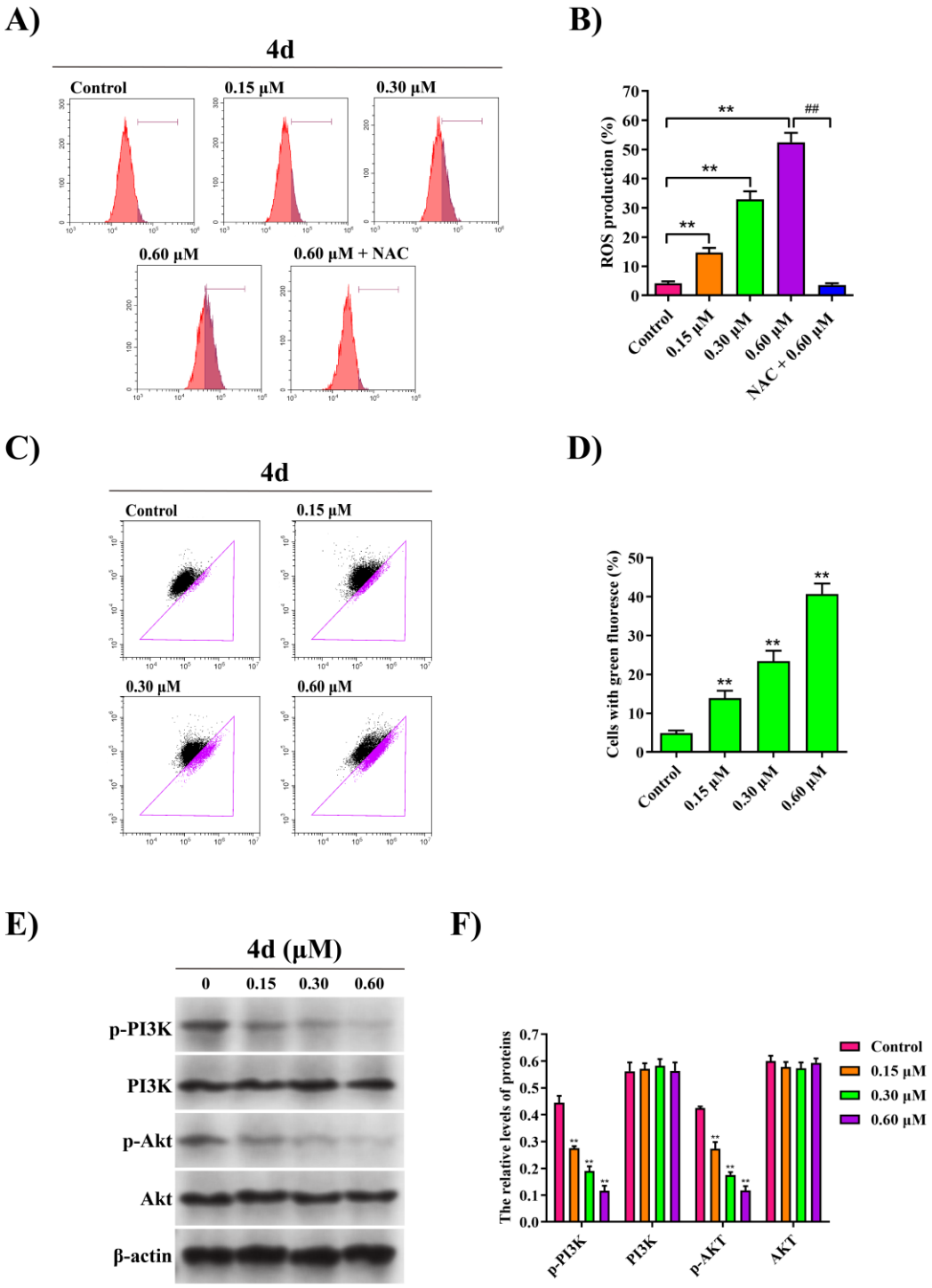

Figure 6. Compound **4d** promoted ROS-mediated PI3K/Akt-mitochondrial pathway. (A) Representative images of ROS induction analyzed by flow cytometry. (B) Histograms display ROS-positive cell percentages. (C) Representative images of cells with MMP analyzed by flow cytometry. (D) Histograms display the percentages of cells with collapsed MMP. (E) Western blot analysis of indicated proteins with *β*-actin as internal reference. (F) Histograms display the density ratios of *p*-PI3K, PI3K, *p*-Akt and Akt to *β*-actin. Data are expressed as the mean ± SD (n = 3). $^{**}p < 0.01$ *vs*. control group. $^{\#\#}p < 0.01$ *vs*. 0.60 μM **4d**-treated group.

The PI3K/Akt pathway plays key roles in cancer cell proliferation and apoptosis[41], and could be regulated by induction of ROS[42]. Some recent studies demonstrated that berberine induced apoptosis by inhibiting the PI3K/Akt pathway[43-45]. Thus, the effect of **4d** on PI3K/Akt pathway was examined in HepG2 cells by western blot analysis (Figure 6E). After incubating with **4d** at concentrations of 0~0.60 μM, the expression levels of *p*-PI3K and *p*-Akt significantly decreased in dose-dependent manners, while the total protein levels of PI3K and Akt were not obviously altered (Figure 6F). The results indicated that **4d** induced HepG2 cell apoptosis possibly via promoting ROS-medicated PI3K/Akt pathway.

2.10. Pharmacokinetic properties of compound 4d

Considering the excellent *in vitro* anti-HCC activity, the pharmacokinetic profile of compound **4d** was further investigated *in vivo*. Male SD rats were injected intravenously with 1 mg/kg of **4d**. The results were summarized in Table 4. The half-life ($T_{1/2}$) and mean residence time (MRT_{0-t}) of **4d** were 2.62 h and 1.81 h, respectively. Moreover, the plasma concentration (C_0) of **4d** was 872 ng/mL after dosing and decreased to 758 ng/mL after 5 min. In addition, the area under the concentration-time curve (AUC_{0-t}) and plasma clearance (CL) of **4d** were separately 674 ng∗h/mL and 1301 mL/h/kg.

Table 4. *In vivo* pharmacokinetic properties of compound **4d**

Compd	$T_{1/2}$ (h)	C_0 (ng/mL)	C_{5min} (ng/mL)	MRT_{0-t} (h)	AUC_{0-t} (ng∗h/mL)	CL (mL/h/kg)
4d	2.62	872	758	1.81	674	1301

2.11. Anti-HCC activity of compound 4d in mouse xenograft model

The *in vivo* anti-HCC activity of compound **4d** was finally examined in the H22 liver cancer xenograft mouse model with cyclophosphamide (CP) as positive reference. As illustrated in Figure 7A-C, after treatment with 10 and 20 mg/kg of **4d** by intravenous injection for 21 days, the tumor volumes and weights were dose-dependently reduced with tumor inhibition rates (TIRs) of 51.8% and 62.9% (*w/w)*, respectively, which was superior to that of berberine (**1**, TIR 42.3%, *w*/*w*) even at a lower dose of 10 mg/kg and comparable to positive reference CP at the same dose of 20 mg/kg. Besides, mice body weights were not reduced during treatment with **4d** (Figure 7D). Furthermore, the H&E staining showed that there were no observable organ-associated toxicities after treatment with 20 mg/kg of **4d** except CP with little toxicity (Figure 7E).

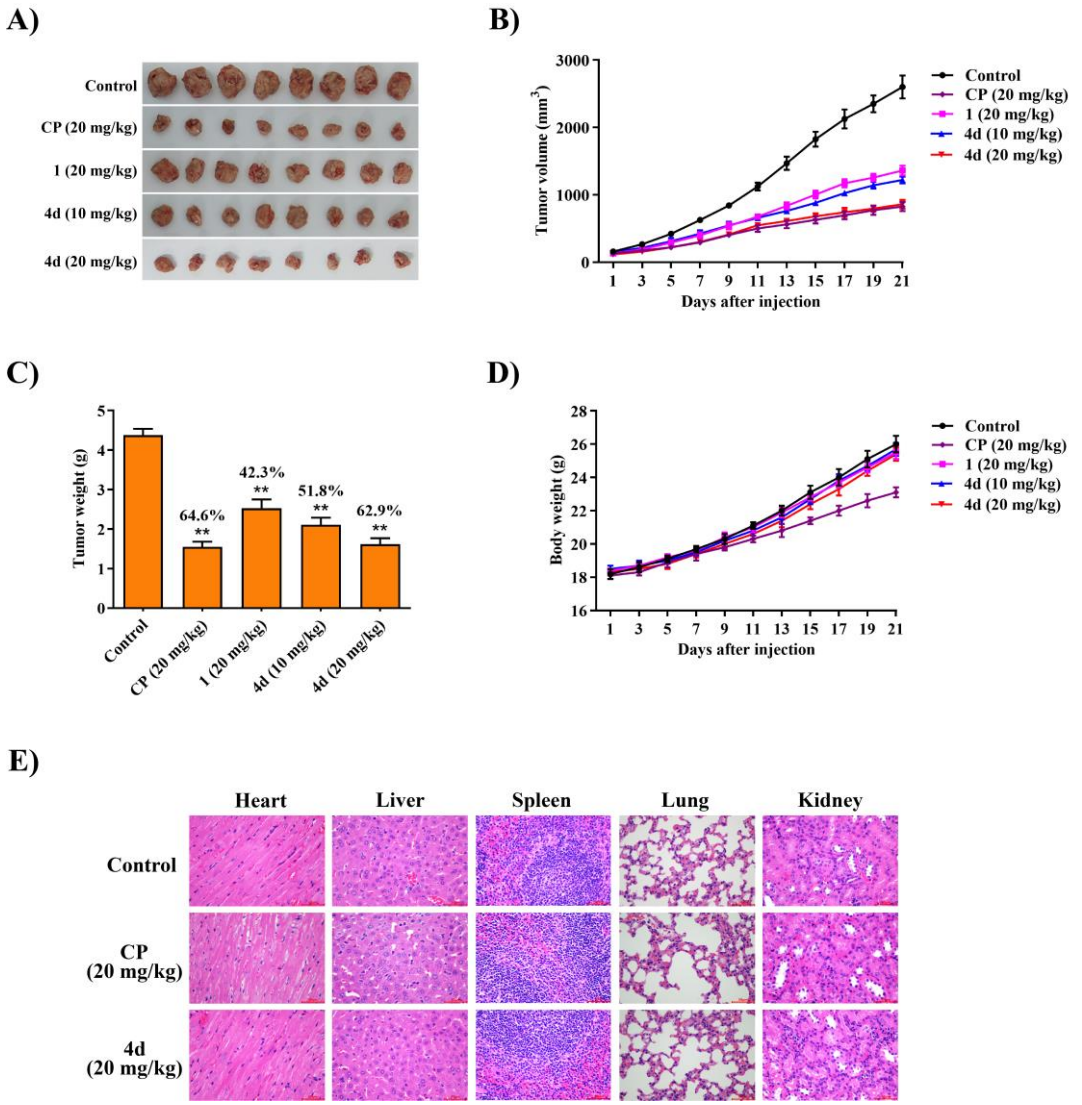

Figure 7. *In vivo* anti-HCC activity of compound **4d** in the H22 liver cancer xenograft mouse model. (A) Images of excised tumors from mice after treatment of 21 days. (B) Tumor volume changes during treatment. (C) Weight of the excised tumors of each group. (D) Body weight changes of mice during treatment. (E) H&E staining images of heart, liver, spleen, lung, and kidney of mice collected from control, CP and **4d** groups. Scale bar = 50 μm. CP: cyclophosphamide. Data are expressed as the mean ± SD (n = 8). $^{**}P < 0.01$ *vs*. control group.

3. Conclusion

In summary, a series of novel 9-*N*-substituted-13-alkylberberine derivatives were further designed, prepared based on our previous studies, and all the newly obtained derivatives showed notably enhanced antiproliferative activity against HepG2 cells compared to parent compound berberine, comparable or even superior to positive control cisplatin. The optimal compound **4d** exhibited potent anti-HCC activity against four human hepatoma cell lines with IC_{50} values of 0.58~1.15 μM. More importantly, **4d** displayed more than 40-fold higher activity against cisplatin-resistant hepatoma HepG2/DPP cells while possessing lower cytotoxicity against normal hepatic LX-2 cells.

Subsequently, the mechanism studies revealed that compound **4d** selectively stabilized and induced G4 DNA formation, which led to *c*-MYC expression downregulation in HepG2 cells. Besides, **4d** inhibited HepG2 cell proliferation by blocking G2/M-phase cell cycle with related protein (*e.g. p*-cdc25c, cdc2, cyclin B1) expression alterations. Additionally, **4d** induced apoptosis of HepG2 cells by a ROS-promoted PI3K/Akt-mitochondrial apoptotic pathway with corresponding changes in the expressions of related proteins such as Bax, Bcl-2, cytochrome C, caspase-3, *p*-PI3K and *p*-Akt.

Furthermore, compound **4d** possessed good pharmacokinetic properties by intravenous injection. And in the same mode of administration, **4d** dose-dependently significantly suppressed the tumor growth (both volume and weight) in the H22 liver cancer xenograft mouse model, with a TIR of 62.9% (*w/w*), which was much superior to that of berberine (TIR: 42.3%, *w/w*) and even comparable to positive reference CP at the same dose. Meanwhile, **4d** had no observable toxic effect during/after treatment.

Collectively, the newly discovered 9,13-disubstituted berberine derivative **4d** showed excellent anti-HCC profiles both *in vitro* and *in vivo*, and has the potential to be further developed into a promising anti-HCC candidate from Chinese medicine.

4. Experimental section

4.1. Chemistry

4.1.1. General methods

Most commercially available chemical reagents or solvents were directly used unless indicated otherwise. The spectra ($^1H/^{13}C$ NMR) data were obtained by a Bruker-300 spectrometer (Bruker Company, Germany). $CDCl_3$ was employed as solvents with TMS as internal reference. δ values (ppm) show the chemical shifts with J values (H_Z) as the coupling constants. An Agilent QTOF 6520 mass spectrometer (Agilent Tech, USA) was used to measure HRMS with ESI as the ion source. Purities of representative compounds were determined by HPLC (SHIMADZU LabSolutions, Japan) on an Agilent C18 column (0.46 cm × 15 cm, 5 μm, λ = 265 nm, 1 mL/min) using CH_3CN/0.05% $NaH_2PO_{4(aq)}$ (60/40) as an eluent. The thin-layer chromatography (TLC, GF254, 0.25 mm) was used to monitor the reactions by UV visualization. Commercial Al_2O_3 (neutral, 100-300 mesh, Qingdao Haiyang Chemical, China) was purchased for flash column chromatography. Compounds **3a-d** were prepared by our reported methods[30].

4.1.2. General procedure for the syntheses of compounds 4 and 5

Compound **3a** (0.2 mmol) and amine/aminoethanol (0.6 mmol) were added in dry acetonitrile (2 mL), and stirred at reflux for 7-12 h. After removing the reaction solvent under reduced pressure, the resulting mixture underwent the purification by neutral Al_2O_3 column chromatography with an eluent of dichloromethane/methanol to afford the title compound.

9-((2-Aminoethyl)amino)-10-methoxy-13-octyl-5,6-dihydro-[1,3]dioxolo[4,5-*g*]isoquinolino[3,2-*a*]isoquinolin-7-ium chloride (**4a**) Red solid in 27% yield (28 mg). m.p. 130 – 132 °C. ^1H NMR (300 MHz, CDCl3) δ 10.92 (s, 1H), 7.56 (d, *J* = 8.8 Hz, 1H),

7.37 (d, *J* = 8.9 Hz, 1H), 7.02 (s, 2H), 6.81 (s, 1H), 6.04 (s, 2H), 4.91 (s, 2H), 4.16 – 3.92 (m, 7H), 3.17 – 3.09 (m, 4H), 3.04 – 2.97 (m, 2H), 1.84 – 1.73 (m, 2H), 1.48 – 1.41 (m, 2H), 1.37 – 1.25 (m, 8H), 0.85 (t, *J* = 6.5 Hz, 3H). ^{13}C NMR (75 MHz, $CDCl_3$) δ 149.2, 147.3, 147.1, 146.0, 138.7, 134.2, 133.4, 133.1, 123.9, 120.8, 118.1, 113.3, 109.1, 108.5, 102.0, 56.9, 56.6, 47.9, 41.9, 31.8, 30.6, 29.72, 29.66, 29.2, 29.1, 28.9, 22.6, 14.1. HRMS (ESI) calculated for $C_{29}H_{38}ClN_3O_3$ $[M\text{-}Cl]^+$ 476.2908, found 476.2920.

9-((3-Aminopropyl)amino)-10-methoxy-13-octyl-5,6-dihydro-[1,3]dioxolo[4,5-*g*] isoquinolino[3,2-*a*]isoquinolin-7-ium chloride (**4b**) Red solid in 31% yield (33 mg). m.p. 123 – 125 °C. ^{1}H NMR (300 MHz, $CDCl_3$) δ 10.97 (s, 1H), 7.54 (d, *J* = 8.9 Hz, 1H), 7.31 (d, *J* = 8.9 Hz, 1H), 7.11 (s, 1H), 7.03 (s, 1H), 6.81 (s, 1H), 6.04 (s, 2H), 4.91 (s, 2H), 3.92 (s, 3H), 3.89 – 3.80 (m, 4H), 3.13 – 3.08 (m, 2H), 3.01 – 2.93 (m, 4H), 2.01 – 1.97 (m, 2H), 1.83 – 1.75 (m, 2H), 1.47 – 1.40 (m, 2H), 1.38 – 1.21 (m, 8H), 0.86 – 0.82 (m, 3H). ^{13}C NMR (75 MHz, $CDCl_3$) δ 149.3, 147.1, 146.6, 145.7, 139.6, 134.0, 133.4, 133.2, 133.0, 123.7, 120.8, 117.3, 112.3, 109.1, 108.5, 102.0, 56.9, 56.6, 44.3, 38.7, 32.4, 31.8, 30.6, 29.8, 29.6, 29.2, 29.1, 29.0, 22.6, 14.1. HRMS (ESI) calculated for $C_{30}H_{40}ClN_3O_3$ $[M\text{-}Cl]^+$ 490.3064, found 490.3073.

9-((4-Aminobutyl)amino)-10-methoxy-13-octyl-5,6-dihydro-[1,3]dioxolo[4,5-*g*]i soquinolino[3,2-*a*]isoquinolin-7-ium chloride (**4c**) Red solid in 25% yield (27 mg). m.p. 113 – 115 °C. ^{1}H NMR (300 MHz, $CDCl_3$) δ 11.29 (s, 1H), 7.54 (d, *J* = 8.9 Hz, 1H), 7.42 (s, 1H), 7.27 (d, *J* = 8.9 Hz, 1H), 7.08 (s, 1H), 6.84 (s, 1H), 6.08 (s, 2H), 4.96 (s, 2H), 3.93 (s, 3H), 3.87 – 3.76 (m, 4H), 3.17 – 3.11 (m, 2H), 3.02 – 2.98 (m, 2H), 2.79 – 2.70 (m, 2H), 1.86 – 1.77 (m, 4H), 1.65 – 1.56 (m, 2H), 1.53 – 1.43 (m, 2H), 1.38 – 1.28 (m, 8H), 0.90 – 0.86 (m, 3H). ^{13}C NMR (75 MHz, $CDCl_3$) δ 149.2, 147.0, 146.4, 145.6, 139.8, 133.9, 133.3, 133.0 (2), 123.9, 120.8, 117.1, 111.8, 109.0, 108.4, 102.0, 56.9, 56.3, 46.7, 41.3, 31.7, 30.5, 29.7, 29.64, 29.56, 29.2, 29.0, 28.3, 22.6, 14.1. HRMS (ESI) calculated for $C_{31}H_{42}ClN_3O_3$ $[M\text{-}Cl]^+$ 504.3221, found 504.3222.

9-((2-(Dimethylamino)ethyl)amino)-10-methoxy-13-octyl-5,6-dihydro-[1,3]diox olo[4,5-*g*]isoquinolino[3,2-*a*]isoquinolin-7-ium chloride (**4d**) Red solid in 42% yield (45 mg). m.p. 95 – 97 °C. ^{1}H NMR (300 MHz, $CDCl_3$) δ 11.27 (s, 1H), 7.63 (d, *J* = 9.1 Hz, 1H), 7.46 – 7.43 (m, 2H), 7.08 (s, 1H), 6.85 (s, 1H), 6.09 (s, 2H), 4.93 (s, 2H), 4.22 – 4.16 (m, 2H), 4.04 (s, 3H), 3.51 (t, *J* = 5.7 Hz, 2H), 3.19 – 3.14 (m, 2H), 3.02 (t, *J* = 5.3 Hz, 2H), 2.89 (s, 6H), 1.88 – 1.78 (m, 2H), 1.53 – 1.44 (m, 2H), 1.38 – 1.22 (s, 8H), 0.90 – 0.86 (m, 3H). ^{13}C NMR (75 MHz, $CDCl_3$) δ 149.2, 147.1, 146.6, 146.0, 139.1, 133.8, 133.12, 133.10, 132.7, 123.3, 120.7, 117.2, 112.6, 109.0, 108.4, 102.0, 59.2, 56.8, 56.3, 45.0, 44.2, 31.7, 30.5, 29.7, 29.5, 29.1, 29.0, 28.9, 22.5, 14.0. HRMS (ESI) calculated for $C_{31}H_{42}N_3O_3$ $[M\text{-}Cl]^+$ 504.3221, found 504.3231. HPLC purity 98.80% (t_R = 5.889 min).

10-Methoxy-13-octyl-9-((3-(pyrrolidin-1-yl)propyl)amino)-5,6-dihydro-[1,3]dio xolo[4,5-*g*]isoquinolino[3,2-*a*]isoquinolin-7-ium chloride (**4e**) Red solid in 38% yield (44 mg). m.p. 91 – 93 °C. ^{1}H NMR (300 MHz, $CDCl_3$) δ 11.22 (s, 1H), 7.61 (d, *J* = 9.0 Hz, 1H), 7.40 (d, *J* = 9.0 Hz, 1H), 7.13 – 7.10 (m, 2H), 6.85 (s, 1H), 6.10 (s, 2H), 4.94 (s, 2H), 3.99 (s, 3H), 3.90 – 3.84 (m, 2H), 3.57 – 3.52 (m, 2H), 3.20 – 3.14 (m, 2H), 3.02 (t, *J* = 5.2 Hz, 2H), 2.60 (brs, 4H), 2.46 – 2.37 (m, 2H), 2.11 (s, 4H), 1.88 – 1.79

(m, 2H), 1.53 – 1.44 (m, 2H), 1.38 – 1.24 (m, 8H), 0.90 – 0.86 (m, 3H). ^{13}C NMR (75 MHz, $CDCl_3$) δ 149.4, 147.3, 146.8, 145.5, 138.9, 134.0, 133.5, 133.04, 132.98, 124.1, 120.7, 117.5, 113.2, 109.1, 108.5, 102.1, 56.9, 56.5, 53.5, 53.4, 44.4, 31.8, 30.7, 29.8, 29.6, 29.2, 29.04, 28.99, 27.1, 23.4, 22.6, 14.1. HRMS (ESI) calculated for $C_{34}H_{46}N_3O_3$ $[M\text{-}Cl]^+$ 544.3534, found 544.3537. HPLC purity 98.795% (t_R = 5.615 min).

10-Methoxy-9-((3-morpholinopropyl)amino)-13-octyl-5,6-dihydro-[1,3]dioxolo[4,5-*g*]isoquinolino[3,2-*a*]isoquinolin-7-ium chloride (**4f**) Red solid in 32% yield (38 mg). m.p. 92 – 94 °C. ^{1}H NMR (300 MHz, $CDCl_3$) δ 11.25 (s, 1H), 7.55 (d, *J* = 8.9 Hz, 1H), 7.29 (d, *J* = 8.9 Hz, 1H), 7.26 (s, 1H), 7.08 (s, 1H), 6.85 (s, 1H), 6.09 (s, 2H), 4.98 (s, 2H), 3.95 (s, 3H), 3.87 (t, *J* = 6.5 Hz, 2H), 3.74 (t, *J* = 4.6 Hz, 4H), 3.17 – 3.12 (m, 2H), 3.00 (t, *J* = 5.5 Hz, 2H), 2.66 – 2.61 (m, 2H), 2.57 (s, 4H), 2.08 – 1.93 (m, 2H), 1.89 – 1.79 (m, 2H), 1.54 – 1.44 (m, 2H), 1.39 – 1.24 (m, 8H), 0.91 – 0.86 (m, 3H). ^{13}C NMR (75 MHz, $CDCl_3$) δ 149.3, 147.1, 146.3, 145.8, 140.0, 133.8, 133.1, 133.0, 132.9, 123.7, 120.8, 116.9, 111.8, 109.1, 108.4, 102.0, 66.4, 56.9, 56.6, 56.2, 53.4, 45.6, 31.8, 30.5, 29.75, 29.67, 29.6, 29.2, 29.0, 27.5, 22.6, 14.1. HRMS (ESI) calculated for $C_{34}H_{46}N_3O_4$ $[M\text{-}Cl]^+$ 560.3483, found 560.3493. HPLC purity 98.786% (t_R = 6.755 min).

9-((2-Hydroxyethyl)amino)-10-methoxy-13-octyl-5,6-dihydro-[1,3]dioxolo[4,5-*g*]isoquinolino[3,2-*a*]isoquinolin-7-ium chloride (**5**) Red solid in 51% yield (52 mg). m.p. 115 – 117 °C. ^{1}H NMR (300 MHz, $CDCl_3$) δ 11.35 (s, 1H), 7.59 (d, *J* = 9.0 Hz, 1H), 7.36 (d, *J* = 9.0 Hz, 1H), 7.09 (s, 1H), 6.85 (s, 1H), 6.75 (t, *J* = 4.5 Hz, 1H), 6.09 (s, 2H), 5.22 (t, *J* = 6.3 Hz, 1H), 4.97 (s, 2H), 3.98 – 3.93 (m, 5H), 3.92 – 3.86 (m, 2H), 3.20 – 3.14 (m, 2H), 3.00 (t, *J* = 5.6 Hz, 2H), 1.87 – 1.78 (m, 2H), 1.53 – 1.44 (m, 2H), 1.38 – 1.24 (m, 8H), 0.90 – 0.86 (m, 3H). ^{13}C NMR (75 MHz, $CDCl_3$) δ 149.3, 147.2, 147.0, 145.5, 139.8, 134.0, 133.4, 133.1, 133.0, 124.5, 120.7, 117.5, 112.8, 109.1, 108.4, 102.1, 61.2, 57.1, 56.3, 50.8, 31.7, 30.6, 29.7, 29.5, 29.2, 29.01, 28.96, 22.6, 14.1. HRMS (ESI) calculated for $C_{29}H_{37}ClN_2O_4$ $[M\text{-}Cl]^+$ 477.2748, found 477.2758. HPLC purity 99.099% (t_R = 7.594 min).

4.1.3. General procedure for the syntheses of compounds 6a and 6b

N,*N'*-dimethylethylenediamine or 2-aminoethanol (0.6 mmol) was added to a solution of **3a** (0.2 mmol) in anhydrous ethanol (2 mL), and stirred at reflux for 18 h. After removing the reaction solvent under reduced pressure, the resulting mixture underwent the purification by neutral Al_2O_3 column chromatography with an eluent of dichloromethane/methanol to give the title compound.

1-(2-(Dimethylamino)ethyl)-15-methoxy-12-octyl-5,6-dihydro-1*H*-[1,3]dioxolo[4',5':6,7]isoquinolino[2,1-*a*]benzo[*de*][1,6]naphthyridin-4-ium chloride (**6a**) Yellow solid in 23% yield (26 mg). m.p. 87 – 89 °C. ^{1}H NMR (300 MHz, $CDCl_3$) δ 8.49 (d, *J* = 7.3 Hz, 1H), 7.59 (d, *J* = 9.0 Hz, 1H), 7.46 (d, *J* = 9.0 Hz, 1H), 7.23 (d, *J* = 7.3 Hz, 1H), 6.94 (s, 1H), 6.79 (s, 1H), 6.04 (s, 2H), 4.81 (t, *J* = 6.2 Hz, 2H), 4.11 – 4.07 (m, 2H), 4.05 (s, 3H), 2.96 – 2.87 (m, 4H), 2.78 (t, *J* = 6.0 Hz, 2H), 2.32 (s, 6H), 1.73 – 1.63 (m, 2H), 1.44 – 1.37 (m, 2H), 1.30 – 1.22 (m, 8H), 0.87 – 0.83 (m, 3H). ^{13}C NMR (75 MHz, $CDCl_3$) δ 150.2, 149.9, 149.0, 146.8, 145.4, 134.2, 132.6, 129.3, 128.6, 122.9, 122.6, 122.2, 118.1, 117.2, 109.0, 107.9, 101.9, 100.7, 59.3, 57.2, 56.9, 48.3, 45.8, 31.9,

29.8, 29.5, 29.3, 29.2, 29.1, 28.2, 22.7, 14.2. HRMS (ESI) calculated for $C_{33}H_{42}ClN_3O_3$ $[M\text{-}Cl]^+$ 528.3221, found 528.3225. HPLC purity 98.896% (t_R = 6.228 min).

1-(2-Hydroxyethyl)-15-methoxy-12-octyl-5,6-dihydro-1*H*-[1,3]dioxolo[4',5':6,7] isoquinolino[2,1-*a*]benzo[*de*][1,6]naphthyridin-4-ium chloride (**6b**) Yellow solid in 21% yield (23 mg). m.p. 104 – 106 °C. ^{1}H NMR (300 MHz, $CDCl_3$) δ 8.83 (d, *J* = 6.8 Hz, 1H), 7.55 (d, *J* = 8.8 Hz, 1H), 7.47 (d, *J* = 8.7 Hz, 1H), 6.99 (s, 1H), 6.82 (s, 1H), 6.56 (d, *J* = 6.9 Hz, 1H), 6.07 (s, 2H), 5.34 (t, *J* = 5.8 Hz, 1H), 5.10 (s, 2H), 4.02 – 3.99 (m, 5H), 3.90 – 3.85 (m, 2H), 2.97 – 2.89 (m, 4H), 1.79 – 1.60 (m, 2H), 1.48 – 1.42 (m, 2H), 1.30 – 1.18 (m, 8H), 0.89 (t, *J* = 6.6 Hz, 3H). ^{13}C NMR (75 MHz, $CDCl_3$) δ 151.2, 150.0, 149.0, 146.8, 145.8, 133.9, 132.3, 129.5, 128.4, 123.2, 122.5, 122.4, 117.9, 117.3, 109.0, 107.9, 101.9, 98.7, 61.8, 61.3, 57.0, 47.8, 31.9, 29.8, 29.6, 29.4, 29.2, 29.1, 28.1, 22.7, 14.2. HRMS (ESI) calculated for $C_{31}H_{37}ClN_2O_4$ $[M\text{-}Cl]^+$ 501.2748, found 501.2748.

4.1.4. General procedure for the syntheses of compounds 7 and 8

Compounds **7** and **8** were prepared with **3b-d** instead of **3a** by the same method as **4** and **5**, respectively.

9-((2-(Dimethylamino)ethyl)amino)-13-hexyl-10-methoxy-5,6-dihydro-[1,3]diox olo[4,5-*g*]isoquinolino[3,2-*a*]isoquinolin-7-ium chloride (**7a**) Red solid in 41% yield (42 mg). m.p. 84 – 86 °C. ^{1}H NMR (300 MHz, $CDCl_3$) δ 11.09 (s, 1H), 7.57 (d, *J* = 9.0 Hz, 1H), 7.35 (d, *J* = 9.0 Hz, 1H), 7.25 – 7.21 (m, 1H), 7.05 (s, 1H), 6.83 (s, 1H), 6.07 (s, 2H), 4.94 (s, 2H), 4.04 – 3.97 (m, 5H), 3.16 – 3.11 (m, 2H), 3.01 – 2.97 (m, 4H), 2.52 (s, 6H), 1.86 – 1.77 (m, 2H), 1.52 – 1.43 (m, 2H), 1.36 – 1.31 (m, 4H), 0.89 (t, *J* = 6.7 Hz, 3H). ^{13}C NMR (75 MHz, $CDCl_3$) δ 149.4, 147.2, 146.7, 146.2, 139.2, 134.0, 133.25, 133.18, 133.0, 123.6, 120.8, 117.4, 112.6, 109.1, 108.5, 102.1, 59.2, 57.0, 56.4, 45.0, 43.9, 31.3, 30.6, 29.8, 29.4, 29.0, 22.7, 14.1. HRMS (ESI) calculated for $C_{29}H_{38}N_3O_3$ $[M\text{-}Cl]^+$ 476.2908, found 476.2931.

13-Decyl-9-((2-(dimethylamino)ethyl)amino)-10-methoxy-5,6-dihydro-[1,3]diox olo[4,5-*g*]isoquinolino[3,2-*a*]isoquinolin-7-ium chloride (**7b**). Red solid in 37% yield (42 mg). m.p. 82 – 84 °C. ^{1}H NMR (300 MHz, $CDCl_3$) δ 11.19 (s, 1H), 7.59 (d, *J* = 9.0 Hz, 1H), 7.37 (d, *J* = 9.0 Hz, 1H), 7.35 – 7.31 (m, 1H), 7.08 (s, 1H), 6.84 (s, 1H), 6.08 (s, 2H), 4.96 (s, 2H), 4.07 (dt, *J* = 5.9, 5.9 Hz, 2H), 3.99 (s, 3H), 3.18 – 3.11 (m, 4H), 3.03 – 2.99 (m, 2H), 2.62 (s, 6H), 1.88 – 1.78 (m, 2H), 1.52 – 1.43 (m, 2H), 1.38 – 1.23 (m, 12H), 0.87 (t, *J* = 6.6 Hz, 3H). ^{13}C NMR (75 MHz, $CDCl_3$) δ 149.4, 147.2, 146.9, 146.2, 138.7, 134.1, 133.3, 133.2, 133.0, 123.8, 120.8, 117.7, 113.2, 109.2, 108.5, 102.1, 58.8, 57.0, 56.5, 44.6, 43.3, 31.9, 30.7, 29.8, 29.7, 29.59, 29.58, 29.3, 29.1, 29.0, 22.7, 14.2. HRMS (ESI) calculated for $C_{33}H_{46}N_3O_3$ $[M\text{-}Cl]^+$ 532.3534, found 532.3541.

9-((2-(Dimethylamino)ethyl)amino)-13-dodecyl-10-methoxy-5,6-dihydro-[1,3]di oxolo[4,5-*g*]isoquinolino[3,2-*a*]isoquinolin-7-ium chloride (**7c**) Red solid in 45% yield (54 mg). m.p. 83 – 85 °C. ^{1}H NMR (300 MHz, $CDCl_3$) δ 11.01 (s, 1H), 7.54 (d, *J* = 9.0 Hz, 1H), 7.31 (d, *J* = 9.0 Hz, 1H), 7.13 (t, *J* = 5.6 Hz, 1H), 7.02 (s, 1H), 6.79 (s, 1H), 6.03 (s, 2H), 4.91 (s, 2H), 3.96 – 3.90 (m, 5H), 3.12 – 3.07 (m, 2H), 2.98 – 2.95 (m, 2H), 2.84 (t, *J* = 6.1 Hz, 2H), 2.40 (s, 6H), 1.82 – 1.72 (m, 2H), 1.48 – 1.38 (m, 2H), 1.33 – 1.20 (m, 16H), 0.81 (t, *J* = 6.6 Hz, 3H). ^{13}C NMR (75 MHz, $CDCl_3$) δ 149.2, 147.1, 146.5, 146.0, 139.3, 133.9, 133.2, 133.1, 132.8, 123.4, 120.8, 117.2, 112.4, 109.1,

108.4, 102.0, 59.3, 56.9, 56.3, 45.1, 44.2, 31.9, 30.5, 29.74, 29.67, 29.60, 29.57, 29.55, 29.3, 29.1, 29.0, 22.7, 14.1. HRMS (ESI) calculated for $C_{35}H_{50}ClN_3O_3$ $[M\text{-}Cl]^+$ 560.3847, found 560.3857.

13-Hexyl-9-((2-hydroxyethyl)amino)-10-methoxy-5,6-dihydro-[1,3]dioxolo[4,5-*g*]isoquinolino[3,2-*a*]isoquinolin-7-ium chloride (**8a**) Red solid in 48% yield (47 mg). m.p. 136 – 138 °C. ^{1}H NMR (300 MHz, $CDCl_3$) δ 11.35 (s, 1H), 7.60 (d, *J* = 9.0 Hz, 1H), 7.37 (d, *J* = 9.0 Hz, 1H), 7.09 (s, 1H), 6.86 (s, 1H), 6.74 (t, *J* = 4.8 Hz, 1H), 6.10 (s, 2H), 5.23 (s, 1H), 4.97 (s, 2H), 3.99 – 3.94 (m, 5H), 3.92 – 3.87 (m, 2H), 3.20 – 3.14 (m, 2H), 3.00 (t, *J* = 5.7 Hz, 2H), 1.89 – 1.82 (m, 2H), 1.55 – 1.45 (m, 2H), 1.38 – 1.34 (m, 4H), 0.91 (t, *J* = 6.9 Hz, 3H). ^{13}C NMR (75 MHz, $CDCl_3$) δ 149.3, 147.2, 147.0, 145.4, 139.7, 134.0, 133.4, 133.1, 133.0, 124.4, 120.7, 117.6, 112.9, 109.1, 108.4, 102.1, 61.2, 57.1, 56.3, 50.8, 31.2, 30.5, 29.8, 29.2, 28.9, 22.6, 14.0. HRMS (ESI) calculated for $C_{27}H_{33}N_2O_4$ $[M\text{-}Cl]^+$ 449.2435, found 449.2438.

13-Decyl-9-((2-hydroxyethyl)amino)-10-methoxy-5,6-dihydro-[1,3]dioxolo[4,5-*g*]isoquinolino[3,2-*a*]isoquinolin-7-ium chloride (**8b**) Red solid in 45% yield (49 mg). m.p. 131 – 133 °C. ^{1}H NMR (300 MHz, $CDCl_3$) δ 11.36 (s, 1H), 7.60 (d, *J* = 9.0 Hz, 1H), 7.37 (d, *J* = 9.0 Hz, 1H), 7.09 (s, 1H), 6.86 (s, 1H), 6.74 (t, *J* = 4.8 Hz, 1H), 6.10 (s, 2H), 5.23 (s, 1H), 4.97 (s, 2H), 3.98 – 3.87 (m, 7H), 3.20 – 3.14 (m, 2H), 3.00 (t, *J* = 5.5 Hz, 2H), 1.89 – 1.80 (m, 2H), 1.53 – 1.44 (m, 2H), 1.47 – 1.21 (m, 10H), 0.88 (t, *J* = 6.6 Hz, 3H). ^{13}C NMR (75 MHz, $CDCl_3$) δ 149.4, 147.3, 147.0, 145.6, 140.0, 134.1, 133.4, 133.2, 133.1, 124.6, 120.8, 117.6, 112.7, 109.2, 108.5, 102.1, 61.3, 57.2, 56.4, 50.9, 31.9, 30.7, 29.84, 29.76, 29.7, 29.6, 29.3, 29.2, 29.1, 22.7, 14.2. HRMS (ESI) calculated for $C_{31}H_{41}ClN_2O_4$ $[M\text{-}Cl]^+$ 505.3061, found 505.3071.

13-Dodecyl-9-((2-hydroxyethyl)amino)-10-methoxy-5,6-dihydro-[1,3]dioxolo[4,5-*g*]isoquinolino[3,2-*a*]isoquinolin-7-ium chloride (**8c**) Red solid in 41% yield (47 mg). m.p. 125 – 127 °C. ^{1}H NMR (300 MHz, $CDCl_3$) δ 11.31 (s, 1H), 7.60 (d, *J* = 9.0 Hz, 1H), 7.37 (d, *J* = 9.0 Hz, 1H), 7.09 (s, 1H), 6.85 (s, 1H), 6.72 (t, *J* = 4.5 Hz, 1H), 6.09 (s, 2H), 5.22 (s, 1H), 4.96 (s, 2H), 3.98 – 3.86 (m, 7H), 3.19 – 3.14 (m, 2H), 3.00 (t, *J* = 5.6 Hz, 2H), 1.88 – 1.78 (s, 2H), 1.53 – 1.44 (m, 2H), 1.38 – 1.26 (m, 16H), 0.87 (t, *J* = 6.6 Hz, 3H). ^{13}C NMR (75 MHz, $CDCl_3$) δ 149.4, 147.2, 147.1, 145.5, 139.8, 134.1, 133.4, 133.2, 133.1, 124.4, 120.7, 117.6, 112.9, 109.1, 108.5, 102.1, 61.3, 57.1, 56.4, 50.8, 31.9, 30.6, 29.8, 29.7, 29.64, 29.61, 29.58, 29.4, 29.1, 29.0, 22.7, 14.2. HRMS (ESI) calculated for $C_{33}H_{45}N_2O_4$ $[M\text{-}Cl]^+$ 533.3374, found 533.3381.

4.2. Biology

4.2.1. General materials

HepG2, Sk-Hep-1, Hep3B cells from ATCC (Rockville, MD, USA), Huh-7 cell from Glow Biologics (New York, USA), HepG2/DDP cell from Meisen (Zhejiang, China), LX-2 cell from Sunncell (Hubei, China) and H22 cell from Beyotime (Shanghai, China) were separately purchased. MTT and ROS assay kits were purchased from Beyotime (Shanghai, China). The Annexin V/FITC apoptosis and cell cycle detection kits, crystal violet and HE staining reagents were purchased from KeyGEN Biotech (Nanjing, China). MitoProbe™ JC-1 assay kit from Thermo Fisher Scientific (Pittsburgh, PA, USA) and Matrigel Matrix (BD Bioscience, USA) were separately

purchased. Primary antibodies against *p*-cdc25c and cdc2 from CST (Boston, USA), *c*-MYC, cyclin B1, Bax, Bcl-2, cytochrome C, caspase-3 *p*-PI3K, PI3K, *p*-Akt, Akt, MMP-9, *p*-FAK, FAK and *β*-actin from Abcam (Cambridge, UK) were separately purchased. The fluorescent secondary antibodies (goat anti-rabbit or rabbit anti-mouse) were purchased from Abcam (Cambridge, UK). Cisplatin and cyclophosphamide were purchased from Sigma (St. Louis, MO, USA). The DxFlex flow cytometer was purchased from Beckman (Brea, CA, USA).

4.2.2. MTT assay

HepG2, Sk-Hep-1, Huh-7, Hep3B, HepG2/DDP and LX-2 cell lines were separately seeded in 96-well plates and incubated in 5% CO_2 incubator at 37 ℃ for 24 h. After removing the medium, different concentrations of test compounds were added to each well and incubated for 72 h. The MTT reagent (5 mg/mL in PBS) was added and incubated for 4 h, the optical density was measured with a microplate reader (BIO-RAD Instruments Inc NO.550) at 490 nm. The negative reference agent was 0.1% DMSO. The IC_{50} values were calculated according to the dose-dependent curves. All the experiments were repeated in at least three independent experiments.

4.2.3. FRET-melting assay

The oligomers FPu18T (5'-FAM-AGGGTGGGGA-GGGTGGGG-TAMRA-3') and F10T [5'-FAM-dTATAGCTATA-HEG-TATA-GCTATA-TAMRA-3'] (HEG linker: [(-CH_2-CH_2-O-)$_6$]) were separately used as *c*-MYC G4 and duplex DNA model, respectively. The tests were conducted in a Real-Time PCR apparatus (LigntCycler 480, Roche Applied Science). The concentrations of selected oligomers were diluted by Tris-HCl buffer (0.2 mM KCl contained, *p*H 7.2, Sigma) to 0.2 μM. The oligomer melting process was monitored in the presence or absence of 2.0 μM test compounds by detecting the fluorescence intensity of fluorescein. The measurements were independently performed in triplicate with excitation at 470 nm and detection at 530 nm. Fluorescence readings were taken at an interval of 2 ℃ over the range of 30-98 ℃, with a constant temperature being maintained for 1 min prior to each reading. The data were analyzed by GraphPad Prism 8.0 (LaJolla, San Diego, CA). To investigate the selectivity of compounds for the G4s, excess non-fluorescent ds26 DNA (5'-GTTAGCCTAGCTTAAGCTAGGCTAAC-3', 10 μM) was added, followed by the same method as above.

4.2.4. Molecular docking study

The theoretical binding property of **4d** with *c*-MYC G4 DNA was calculated by AutoDock 4.2. The crystal structure of *c*-MYC G4 DNA (PDB ID: 2L7V) was prepared by adding hydrogens and assigning AD4 atom types in AutoDockTools-1.5.6. The test compound was optimized by Chem3D software to give an initial 3D conformation. During the docking procedure, the receptor was set to be rigid, while the ligand was flexible. Lamarckian Genetic Algorithm was used for conformational search and the parameters "Number of GA Runs" and "Maximum Number of evals" were set to 50 and 25000000, respectively. Other parameters kept default. Finally, ten independent

calculations were performed and the conformation with the lowest binding free energy and the highest frequency among the repetitions was selected for analysis.

4.2.5. Immunocytochemistry assay

HepG2 cells were seeded into six-well plates and incubated at 37 ºC overnight, and then treated with or without 0.3 μM **4d** for another 72 h. Cells were washed with PBS and fixed with ice-cold aceto-methanol (1:1). For immunocytochemistry, cells were then blocked with 3% BSA in PBS, and incubated overnight with BG4 antibody (AntibodySystem, France). DDDDK tag antibody (GeneTex, USA) was add, followed by treatment of secondary goat anti-rabbit antibody. Cells were stained with DAPI solution (KeyGEN Biotech, Nanjing, China). Images were taken in a confocal laser scanning microscope and analyzed by a Fluoview FV-3000 software (Olympus, Japan).

4.2.6. Cell cycle analysis

HepG2 cells were incubated with **4d** as described above. Cells were harvested, washed with cold PBS and then fixed with 70% ethanol at -20 ºC for 12 h. According to the kit's instructions, HepG2 cells were resuspended in PBS containing 100 μL RNase A and 400 μL of PI for 30 min. The cellular DNA content for the cell cycle distribution was measured by DxFlex flow cytometer.

4.2.7. Annexin V-FITC /PI apoptosis detection assay

According to the kit's instructions, briefly, after treatment with or without **4d** at indicated concentrations for 72 h, HepG2 cells were washed twice in PBS, centrifuged and resuspended in 500 μL AnnexinV binding buffer. The cells were then harvested, washed and stained with 5 μL Annexin V-FITC and 5 μL PI in the darkness for 15 min. The percentages of apoptotic cells were determined by DxFlex flow cytometer.

4.2.8. ROS detection assay

ROS level was detected by the peroxide-sensitive fluorescent probe DCF-DA. According to the kit's instructions, briefly, after treatment with different concentrations of **4d** for 72 h, HepG2 cells were incubated with 10 mM DCF-DA at 37 ℃ for 15 min. The intracellular ROS-mediated oxidation of DCF-DA to the fluorescent compound DCF. Then, cells were harvested, and the pellets were suspended in 1 mL PBS. Test compound was analyzed at an excitation wavelength of 480 nm and an emission wavelength of 525 nm by flow cytometry.

4.2.9. JC-1 MMP detection assay

According to the kit's instructions, briefly, after incubation with or without **4d** for 72 h, HepG2 cells were washed in PBS and resuspended in 500 μL JC-1 incubation buffer at 37 ºC for 15 min. Then, different concentrations of **4d** were immediately assessed for red and green fluorescence using a microplate reader (ELx80, Bio-Tek, USA). The fluorescent signal of monomers was measured with an excitation wavelength of 490 nm and an emission wavelength of 535 nm. The percentage of cells with healthy (red) or collapsed (green) mitochondrial membrane potentials was monitored by flow cytometry analysis.

4.2.10. Western blot analysis

HepG2 cells were incubated with **4d** as described above. Cells were collected, centrifuged, and washed twice with ice-cold PBS. The pellet was then resuspended in lysis buffer. After centrifuging lysates for 15 min, the supernatant protein concentration was determined using the BCA protein assay reagents. Equal amounts of protein (20 μg) were resolved using sodium dodecyl sulfate-polyacrylamide gel electrophoresis (SDS-PAGE) and transferred to PVDF membrane. Membranes were blocked for 1 h and then incubated with primary antibodies against *p*-cdc25c, cdc2, cyclin B1, *c*-MYC, Bax, Bcl-2, cytochrome C, caspase-3, *p*-PI3K, PI3K, *p*-Akt, Akt, MMP-9, *p*-FAK, FAK and β-actin at 4 °C overnight. Subsequently, membranes were incubated with fluorescent secondary antibodies (goat anti-rabbit or rabbit anti-mouse) for 1 h and visualized by the enhanced chemiluminescent reagent.

4.2.11. Pharmacokinetic study

Male SD rats (180-220 g, 6-8 weeks) were purchased from Beijing Vital River Laboratory Animal Technology Co. Ltd. After adaptive feeding for one week, the rats were intravenously administrated with 1.0 mg/kg of **4d**. 0.2 mL blood sample was collected via jugular vein at 5 min, 15 min, 30 min, 1 h, 2 h, 4 h, 6 h, 8 h, 12 h and 24 h, respectively. After centrifugating at 6000 r/min, the plasma was separated from blood sample. Then, 100 μL plasma was mixed with 100 μL water, the obtained mixtures were analyzed by LC-MS/MS (ExionLC, SCIEX, USA) after filtering through 0.22 μm membrane. Measurements were made in triplicate independently. HPLC was equipped with a variable wavelength scanning UV detector, quaternary pump and reversed phase C18 column (Waters XBridge BEH, 2.1 mm × 50 mm, 2.5 μm) using acetonitrile/water as an eluent. The flow rate was 0.7 mL/min.

4.2.12. *In vivo* hepatoma xenograft model

Male ICR mice (18-22 g, 5 weeks) were purchased from Shanghai SLAC Laboratory Animals Co. Ltd. The right flank of mice was subcutaneously transplanted with H22 cells (1×10^6 cells/mouse) according to the protocols of tumor transplant research. Mice were weighed and randomly divided into five groups after incubation for one day. Each group was separately intravenously treated with berberine (20 mg/kg), **4d** (10 or 20 mg/kg), CP (20 mg/kg) and control (10% DMF/2% Tween 80/88% saline) for 21 days. The mouse body weights and tumor volumes were measured every 2 days. After the treatments, the mice were sacrificed, the excised tumors were weighed. The tumor volume and TIR (*w*/*w*) were calculated as follows: tumor volume = $L \times W^2/2$, where L is the length and W is the width; TIR (%) = (1-average tumor weight of treated group/average tumor weight of control group) × 100%. All procedures were performed following institutional approval in accordance with the NIH Guide for the Care and Use of Laboratory Animals.

4.2.13. H&E Staining

Mouse organs (heart, liver, spleen, lung, kidney) were isolated and fixed in 4% paraformaldehyde and embedded in paraffin using tissue embedding machine. The tissues were sectioned in the vertical plane into 50 μm-thick and stained with H&E.

Briefly, sections were prepared orderly by dewaxing, staining and dehydration. After staining in Harris hematoxylin solution, sections were stained in eosin-phloxine solution for 1 min and then dehydrated and mounted with neutral resin. The tissue morphology was observed under a microscope (Olympus, Japan).

4.2.14. Statistical analysis

Data from multiple independent experiments are shown as the mean ± SD. Differences between two groups were analyzed by Two-tailed unpaired t test and one-way analysis of variance (ANOVA) were performed by using GraphPad Prism 8.0 (LaJolla, San Diego, CA). $P \leq 0.05$ was considered statistically significant.

Declaration of competing interest

The authors declare that they have no known competing financial interests or personal relationships that could have appeared to influence the work reported in this paper.

Acknowledgments

This study was financially supported by the Jiangsu Specially-Appointed Professors program (No. 013038023001), and Nanjing Science and Technology Innovation Project for Overseas Talents (No. 013062001012).

Appendix A. Supporting information

Supporting data to this article can be found online at https://doi.org/

References

1. Guo M, Jin J, Zhao D, et al. Research advances on anti-cancer natural products. *Front Oncol.* 2022;12:866154.
2. Wang SZ, Dong GQ, Sheng CQ. Structural simplification of natural products. *Chem Rev.* 2019;119:4180-4220.
3. Chen JC, Li WL, Yao HQ, et al. Insights into drug discovery from natural products through structural modification. *Fitoterapia.* 2015;103:231-241.
4. Newman DJ, Cragg GM. Natural products as sources of new drugs over the nearly four decades from 01/1981 to 09/2019. *J Nat Prod.* 2020;83:770-803.
5. Guo ZR. The modification of natural products for medical use. *Acta Pharm Sin B.* 2017;7:119-136.
6. Song DY, Hao JY, Fan DM. Biological properties and clinical applications of berberine. *Front Med -Prc.* 2020;14:564-582.
7. Feng XJ, Sureda A, Jafari S, et al. Berberine in cardiovascular and metabolic diseases: from mechanisms to therapeutics. *Theranostics*. 2019;9:1923-1951.
8. Yang LX, Yu SP, Yang YH, et al. Berberine improves liver injury induced glucose and lipid metabolic disorders via alleviating ER stress of hepatocytes and modulating gut microbiota in mice. *Bioorg Med Chem.* 2022;55:116598.
9. Zhu WQ, Wu HY, Sun ZH, et al. Current evidence and future directions of berberine intervention in depression. *Front Pharmacol.* 2022;13:824420.
10. Cai Y, Xin QQ, Lu JJ, et al. A new therapeutic candidate for cardiovascular diseases: berberine.

Front Pharmacol. 2021;12:631100.
11. Och A, Podgorski R, Nowak R. Biological activity of berberine-A summary update. *Toxins*. 2020;21:713.
12. Xu JH, Long YM, Ni LW, et al. Anticancer effect of berberine based on experimental animal models of various cancers: a systematic review and meta-analysis. *BMC Cancer.* 2019;19:589.
13. Zhou MT, Deng Y, Liu MC, et al. The pharmacological activity of berberine, a review for liver protection. *Eur J Pharmacol.* 2021;890:173655.
14. Liu B, Wang GS, Yang J, et al. Berberine inhibits human hepatoma cell invasion without cytotoxicity in healthy hepatocytes. *PLoS One.* 2011;6:e21416.
15. Yang XL, Huang N. Berberine induces selective apoptosis through the AMPK-mediated mitochondrial/caspase pathway in hepatocellular carcinoma. *Mol Med Rep.* 2013;8:505-510.
16. Devarajan N, Jayaraman S, Mahendra J, et al. Berberine-A potent chemosensitizer and chemoprotector to conventional cancer therapies. *Phytother Res.* 2021;35:3059-3077.
17. Huang Y, Wang K, Gu C, et al. Berberine, a natural plant alkaloid, synergistically sensitizes human liver cancer cells to sorafenib. *Oncol Rep.* 2018;40:1525-1532.
18. Wang KY, Yu GX, Lin JE, et al. Berberine sensitizes human hepatoma cells to regorafenib via modulating expression of circular RNAs. *Front Pharmacol.* 2021;12:632201.
19. Liu CS, Zheng YR, Zhang YF, et al. Research progress on berberine with a special focus on its oral bioavailability. *Fitoterapia.* 2016;109:274-282.
20. Onel B, Lin C, Yang DZ. DNA G-quadruplex and its potential as anticancer drug target. *Sci China Chem*. 2014;57:1605-1614.
21. Kosiol N, Juranek S, Brossart P, et al. G-quadruplexes: A promising target for cancer therapy. *Mol Cancer.* 2021;20:40.
22. Dang CV. MYC on the path to cancer. *Cell.* 2012;149:22-35.
23. Chaudhuri R, Bhattacharya S, Dash J, et al. Recent update on targeting *c*-MYC G-quadruplexes by small molecules for anticancer therapeutics. *J Med Chem.* 2021;64:42-70.
24. Savva L, Georgiades SN. Recent developments in small-molecule ligands of medicinal relevance for harnessing the anticancer potential of G-quadruplexes. *Molecules.* 2021;26:841.
25. Maiti M, Kumar GS. Polymorphic nucleic acid binding of bioactive isoquinoline alkaloids and their role in cancer. *J Nucleic Acids.* 2010;2010:593408.
26. Dickerhoff J, Brundridge N, McLuckey SA, et al. Berberine molecular recognition of the parallel MYC G-quadruplex in solution. *J Med Chem.* 2021;64:6205-6212.
27. Franceschin M, Cianni L, Pitorri M, et al. Natural aromatic compounds as scaffolds to develop selective G-quadruplex ligands: from previously reported berberine derivatives to new palmatine analogues. *Molecules.* 2018;23:1423.
28. Ma Y, Ou TM, Tan JH, et al. Quinolino-benzo-[5,6]-dihydroisoquindolium compounds derived from berberine: A new class of highly selective ligands for G-quadruplex DNA in *c*-myc oncogene. *Eur J Med Chem.* 2011;44:1906-1913.
29. Biffi G, Tannahill D, Miller J, et al. Elevated levels of G-quadruplex formation in human stomach and liver cancer tissues. *PLoS One.* 2014;9:e102711.
30. Chen JC, Duan YP, Yu XX, et al. Development of novel 9-O-substituted-13-octylberberine derivatives as potential anti-hepatocellular carcinoma agents. *J Enzyme Inhib Med Chem.* 2022;37:2423-2433.
31. Wang T, Zou J, Wu Q, et al. Tanshinone IIA derivatives induced S-phase arrest through

stabilizing c-myc G-quadruplex DNA to regulate ROS-mediated PI3K/Akt/mTOR pathway. *Eur J Pharmacol.* 2021;912:174586.

32. Biffi G, Tannahill D, McCafferty J, et al. Quantitative visualization of DNA G-quadruplex structures in human cells. *Nat Chem.* 2013;5:182-186.
33. Murat P, Balasubramanian S. Existence and consequences of G-quadruplex structures in DNA. *Curr Opin Genet Dev.* 2014;25:22-29.
34. Buolamwini J. Cell cycle molecular targets in novel anticancer drug discovery. *Curr Pharm Des.* 2000;6:379-392.
35. Wei ZZ, Qin QP, Meng T, et al. 5-Bromo-oxoisoaporphine platinum(II) complexes exhibit tumor cell cytotoxcicity via inhibition of telomerase activity and disruption of c-myc G-quadruplex DNA and mitochondrial functions. *Eur J Med Chem.* 2018;145:360-369.
36. Zheng CP, Liu YN, Liu Y, et al. Dinuclear ruthenium complexes display loop isomer selectivity to c-MYC DNA G-quadriplex and exhibit anti-tumour activity. *J Inorg Biochem.* 2016;156:122-132.
37. Che T, Chen SB, Tu JL, et al. Discovery of novel schizocommunin derivatives as telomeric G-quadruplex ligands that trigger telomere dysfunction and the deoxyribonucleic acid (DNA) damage response. *J Med Chem.* 2018;61:3436-3453.
38. Circu ML, Aw TY. Reactive oxygen species, cellular redox systems, and apoptosis. *Free Radical Bio Med.* 2010;48:749-762.
39. Zou ZZ, Chang HC, Li HL, et al. Induction of reactive oxygen species: An emerging approach for cancer therapy. *Apoptosis.* 2017;22:1321-1335.
40. Jeong SY, Seol DW. The role of mitochondria in apoptosis. *BMB Rep.* 2008;41:11-22.
41. Jiang NN, Dai QJ, Su XR, et al. Role of PI3K/AKT pathway in cancer: the framework of malignant behavior. *Mol Biol Rep.* 2020;47:4587-4629.
42. Koundouros N, Poulogiannis G. Phosphoinositide 3-kinase/Akt signaling and redox metabolism in cancer. *Front Oncol.* 2018;8:160.
43. Song L, Luo Y, Wang XY, et al. Exploring the active mechanism of berberine against HCC by systematic pharmacology and experimental validation. *Mol Med Rep.* 2019;20:4654-4664.
44. Okuno K, Garg R, Yuan YC, et al. Berberine and oligomeric proanthocyanidins exhibit synergistic efficacy through regulation of PI3K-Akt signaling pathway in colorectal cancer. *Front Oncol.* 2022;12:855860.
45. Li L, Wang XC, Sharvan R, et al. Berberine could inhibit thyroid carcinoma cells by inducing mitochondrial apoptosis, G0/G1 cell cycle arrest and suppressing migration via PI3K-AKT and MAPK signaling pathways. *Biomed Pharmacother.* 2017;95:1225-1231.